

Lisa Träger<sup>1,‡</sup>  
Jan Gläsel<sup>1,‡</sup>  
Marc Scherle<sup>2</sup>  
Julian Hartmann<sup>1</sup>  
Ulrich Nieken<sup>2</sup>  
Bastian J. M. Etzold<sup>1,\*</sup>


# Carbon-Methanol Based Adsorption Heat Pumps: Identifying Accessible Parameter Space with Carbide-Derived Carbon Model Materials

In adsorption heat pumps, the properties of the porous adsorbent and the refrigerant determine the performance. Major parameters for this working pair are the total uptake of the adsorptive, its kinetics, and the heat transfer characteristics. In the technical application despite powdered adsorbents, thin consolidated layers of the adsorbent can be attractive and obtained by a binder-based approach but likely result in competing material properties. Thus, for a process optimization, the accessible parameter space and interdependencies have to be known and were deduced in this work for model porous carbons (carbide-derived carbons derived from TiC and ZrC) and methanol as well as the addition of different amounts of boron nitride, silver, and graphite as heat-conductive agents and the use of two binders.

**Keywords:** Adsorption heat pump, Carbide-derived carbon, Carbon-methanol, Consolidated carbon plate, Model carbon material

*Received:* April 15, 2020; *revised:* May 04, 2020; *accepted:* June 29, 2020

**DOI:** 10.1002/ceat.202000181

 This is an open access article under the terms of the Creative Commons Attribution License, which permits use, distribution and reproduction in any medium, provided the original work is properly cited.



Supporting Information  
available online

## 1 Introduction

Adsorption heat pumps are attractive alternatives to conventional vapor compression cycles due to their effective cooling production while being powered, e.g., with solar or industrial waste heat [1]. However, the low performance in terms of coefficient of performance (COP) and cooling capacity constitute a major drawback [2]. Therefore, over the last decades intensive research activities have been focusing on the improvement of the system performance, e.g., by operational optimization of the adsorption cycle [3–5] and the identification of promising adsorbent-refrigerant pairs [6–16]. In this sense, heat transfer intensification through the adsorbent bed has been considered as one of the most effective methods for the development of high-performance cooling systems due to the poor particle-to-particle heat transfer in powdered systems [2]. In order to overcome this shortcoming, e.g., the adsorption characteristics onto consolidated adsorbent beds based on activated carbon were studied for methanol [17], ethanol [2] or ammonia [18].

It turned out that the composite nature consisting of the active material (activated carbon), binder and potentially a heat-conductive additive is beneficial. The performance of adsorption heat pumps utilizing such consolidated adsorbent beds depends on the heat transfer characteristics, the total uptake of the adsorptive, and its kinetics for the particular composite material. These properties can be influenced by the choice of the porous carbon, the binder, possible additives, and the processing conditions but are strongly interlinked leading to an optimization problem. The complexity for this optimiza-

tion is seen in the high degree of freedom during the material production. It follows that the knowledge about the accessible material parameter space and the interdependencies for such consolidated adsorbents is essential as starting point for an optimization of both the (composite) material and the process.

This study intends to derive the accessible parameter space for the working pair of porous carbon and methanol. Carbide-derived carbons (CDCs) were chosen as adsorbent since their potential as model materials with tunable properties and a high reproducibility during the synthesis has been demonstrated in several applications [19–24]. Two carbides were employed as precursor (TiC and ZrC) and converted to carbon at three different temperatures (800, 1000, and 1200 °C) to vary the carbon properties. As a result, the CDCs allow to span the parameter space for the adsorbent in specific surface area (influencing the total uptake) and degree of crystallinity (influencing the intrinsic heat conductivity). In addition, a commer-

<sup>1</sup>Lisa Träger, Jan Gläsel, Julian Hartmann, Prof. Prof. Dr.-Ing. Bastian J. M. Etzold  
bastian.etzold@tu-darmstadt.de

Technical University of Darmstadt, Department of Chemistry, Ernst-Berl-Institut für Technische und Makromolekulare Chemie, 64287 Darmstadt, Germany.

<sup>2</sup>Marc Scherle, Prof. Dr.-Ing. Ulrich Nieken  
University of Stuttgart, Institute of Chemical Process Engineering, 70199 Stuttgart, Germany.

<sup>‡</sup>These authors contributed equally to this work.

cial activated carbon was also employed in the study for comparison.

The consolidated adsorbent beds were prepared utilizing carboxymethyl cellulose (CMC) and polytetrafluoroethylene (PTFE) as binder. CMC can be employed in very low amounts and results in more brittle structures, whereas for PTFE a higher content is needed, and elastic carbon plates are obtained. Furthermore, three different heat-conductive additives, namely, boron nitride (BN), silver (Ag), and graphite, were utilized in varying amounts up to 50 wt %. The resulting consolidated composites were characterized in terms of effective heat conductivity, specific surface area, methanol adsorption capacity, and uptake kinetics. Additionally, the mechanical stability of the plates was studied to ensure that a sufficient mechanical stability for the application after the fabrication is given.

## 2 Experimental

### 2.1 Material Synthesis

The reactive extraction of titanium carbide (Goodfellow; 50–150  $\mu\text{m}$ ) and zirconium carbide (Goodfellow; max. 45  $\mu\text{m}$ ) was carried out at 800, 1000, and 1200  $^{\circ}\text{C}$  in a horizontal hot-wall reactor setup. Typical conditions were 0.5–2.0  $\text{mol m}^{-3}$  chlorine diluted in helium for ca. 5 h and a superficial gas velocity of 0.03  $\text{m s}^{-1}$  based on reactor temperature and empty tube. After the synthesis, the materials were post-treated in 1  $\text{mol m}^{-3}$  (at 0.03  $\text{m s}^{-1}$ ) hydrogen diluted in helium for 0.5 h at reaction temperature and subsequently cooled down under helium purge. If explicitly stated, the as-received carbide powders were dry-sieved prior to the chlorination to particle fractions of 50–75 and 75–150  $\mu\text{m}$ , respectively.

The sample nomenclature follows the “carbide-CDC-temperature (in  $^{\circ}\text{C}$ )” systematic. For instance, TiC-CDC-1000 50–75  $\mu\text{m}$  was produced at 1000  $^{\circ}\text{C}$  from the precursor TiC with a particle fraction of 50–75  $\mu\text{m}$ . The CDC materials were then mixed with appropriate amounts of sodium carboxymethyl cellulose (CMC; MP Biomedicals, medium viscosity) to obtain a water-based paste with a typical binder content of 2 wt % or an isopropanol-based paste with usually 15 wt % PTFE (MTI Corp.). In certain cases, between 10 and 50 wt % boron nitride (BN; Sigma Aldrich, ca. 1  $\mu\text{m}$ ), silver (Ag; Alfa Aesar, 0.7–1.3  $\mu\text{m}$ ) or graphite powder filed off from a block (C; VWR, naturally occurring) were additionally mixed in the paste as heat-conductive additive. The pasty mixtures were then uniaxially cold-pressed in a hydraulic lab press (Vogt Labormaschinen) at ambient temperature and a surface pressure of 363 bar for 10 min to produce plates with dimensions of ca. 45  $\times$  15  $\times$  2 mm. A commercial activated carbon (VWR Chemicals; charcoal activated (vegetable-based); technical; max. 80  $\mu\text{m}$ ) was processed in the same manner for comparison.

### 2.2 Material Characterization

Field emission scanning microscopy was performed using an HREM XL30 FEG (Philips). If necessary, the samples were sputtered with gold for 100 ms at a potential of 30 mV

(Quorum Technologies; Q300TD). The images were taken at an acceleration voltage of 30 kV. The particle size distributions were determined by laser light scattering using water- or ethanol-based suspensions and a Saturn DigiSizer II (Micromeritics).

The textural properties were determined by low-temperature physisorption analysis at 77 K (Quantachrome; Quadrasorb SI). Beforehand, the samples (powders or small chunks of the plates) were degassed at 120  $^{\circ}\text{C}$  for 22 h under fine vacuum. The characteristic surface area was calculated applying the Brunauer-Emmett-Teller multipoint method (SSA-BET), whereas the total pore volume was determined according to the Gurvich rule. The mean pore diameter (MPD) was assessed from the SSA-BET and total pore volume assuming a slit pore geometry.

Mercury porosimetry was performed on a combined Pascal 140 and Pascal 440 (Thermo Scientific) apparatus. The thermooxidative stability under an oxidizing atmosphere was investigated on a thermogravimetric balance Jupiter STA 449C (Netzsch Gerätebau) by temperature-programmed oxidation between 40 and 1000  $^{\circ}\text{C}$  applying a heating rate of 5  $\text{K min}^{-1}$ . The gas mixture consisted of 20 vol % oxygen and 80 vol % nitrogen.

Raman spectra were recorded from 600 to 3400  $\text{cm}^{-1}$  using a Senterra I microscope spectrometer (Bruker) operated at an incident wavelength of 532 nm. Twelve spectra measured at different spots for each sample were averaged in order to ensure that the results reflect the predominant material character. The data evaluation was carried out with the software Fityk 1.3.1. The effective thermal conductivity of the carbon plates with and without heat-conductive additive was measured via transient hot bridge technique with the aid of a THB 1 (Linseis). Five consecutive analyses with a time span of ca. 30 s in-between were averaged for each sample. The mechanical stability was determined by a 4-point bending test following DIN EN ISO 7438. The core of the self-constructed equipment is a force sensor 8531-5000 from Burster. As stability descriptor, the breaking force was used for the plates prepared with CMC as binder, whereas the applied load at the maximum deformation path was considered for the PTFE-based plates.

### 2.3 Methanol Adsorption and Mass Transfer Studies

The methanol adsorption capacity of different CDC plates was determined at 30 and 90  $^{\circ}\text{C}$  with a self-constructed automated apparatus consisting of a liquid methanol tank and a thermally controlled vapor reservoir coupled to an absolute pressure transducer (MKS Baratron 121A, 1000 mbar). The adsorbed amount is determined according to the static-volumetric mode of operation as described elsewhere [25]. The sample preparation consisted of (i) degassing at 180  $^{\circ}\text{C}$  for 5 h under fine vacuum; (ii) attaching the dried CDC plate to a temperature-controlled sample holder by means of an indium foil (Goodfellow; 0.25 mm) and a liquid MetalPad (Coollaboratory) to provide a reasonable thermal contact; and (iii) subsequent in situ degassing of the fully assembled sample at 90  $^{\circ}\text{C}$  under high vacuum before the measurement.

In addition, the mass transfer properties of different CDC plates were measured with a simplified Wicke-Kallenbach cell

[26]. For this purpose, non-adsorbable gases were passed through the CDC plates by means of a mass flow controller (Bronkhorst EL-Flow Prestige FG-200CV) and the pressure drop across the sample was measured with two absolute pressure gauges (MKS Baratron 627F, P1: 1000 mbar and P2: 100 mbar). Beforehand, the samples were trimmed to match the dimensions of the sample holder and fixed gas-tight with silicone (Wacker Elastosil E10) in order to avoid any bypass flow. The evaluation of the data was performed considering the Dusty-Gas model, i.e., taking Knudsen diffusion and viscous flow into account [27]. Simplified process flow sheets of the adsorption and mass transfer test stand can be found in Figs. S2 and S3 in the Supporting Information.

### 3 Results and Discussion

#### 3.1 Powdered Carbon Active Material

The major component of an adsorbent bed is the active material, which can vary in terms of morphology, textural properties, and carbon microstructure. To obtain a broad variation of these characteristics, as-received TiC and ZrC powders were chlorinated at 800, 1000, and 1200 °C to modulate the properties of the respective CDC materials. The characterization results are compared to the ones of a commercial reference activated carbon (AC).

The reactive extraction of the metal from the carbide is known to be a largely conformal process [28], therefore, for both carbides the morphological characterization by means of laser light scattering and scanning electron microscopy (SEM) imaging was carried out only for the respective CDC material chlorinated at 1000 °C. As can be observed in Fig. 1a, the AC exhibits a nonuniform particle size distribution (PSD) ranging from ca. 1 to 230 μm. The TiC-CDC-1000 particles are in a similar size range, but the distribution has a more log-normal character and a lower fraction of particles smaller than 30 μm compared to the AC. Although the PSD of ZrC-CDC-1000 also shows a weakly developed peak at ca. 80 μm, the particle size of the as-received ZrC powder translates into a predominantly small-sized carbon material with 90% of the particles being smaller than 40 μm (volume-based). Despite differing in terms of PSD, all three carbon materials share one common feature, i.e., an irregular particle shape as evidenced by the SEM imaging (see Fig. S1 in the Supporting Information).

Undoubtedly, one of the most advantageous aspects of the CDC synthesis route is that the chlorination temperature and type of carbide has a decisive influence on the porosity of the obtained carbon material [23, 24, 29, 30], which was studied by nitrogen physisorption analysis. Fig. 1b displays the isotherm of the AC as well as the ones for TiC-CDC- and ZrC-CDC-1000. A summary of the textural characteristics of all CDC materials derived from the as-received carbide powders is presented in Tab. 1.

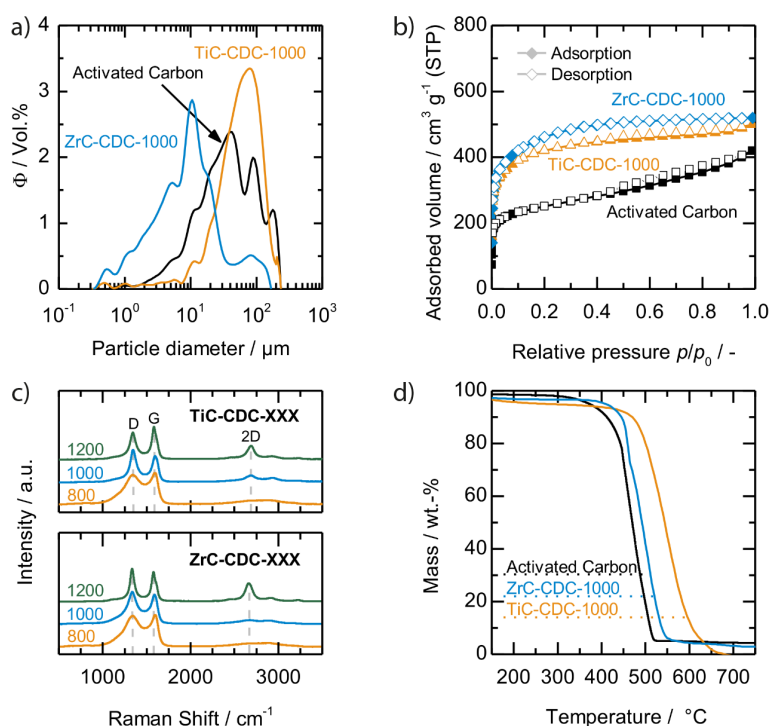


**Figure 1.** Comparison between TiC-CDC-1000, ZrC-CDC-1000, and activated carbon. (a) Volume-based particle size density distribution; (b) nitrogen ad- (closed symbols)/desorption (open symbols) isotherms measured at 77 K in linear scale; (c) Raman spectra; (d) thermogravimetric curves under oxidizing atmosphere of TiC-CDC and ZrC-CDC obtained at different temperatures.

**Table 1.** Summary of the physicochemical properties of TiC-CDC and ZrC-CDC materials synthesized at different temperatures. The data for the activated carbon are also included in the table for comparison.

	Structural properties of powdered samples				
	SSA-BET [m <sup>2</sup> g <sup>-1</sup> ]	V <sub>pore</sub> [mL g <sup>-1</sup> ]	MPD [nm]	T <sub>Onset</sub> [°C]	I <sub>D</sub> /I <sub>G</sub> [-]
Activated carbon	926	0.65	1.40	439	-
<i>TiC-CDC-XXX</i>					
800	1650	0.68	0.82	421	1.13 ± 0.08
1000	1557	0.77	0.99	494	1.22 ± 0.50
1200	1026	0.67	1.30	563	0.76 ± 0.31
<i>ZrC-CDC-XXX</i>					
800	1929	0.83	0.86	457	1.13 ± 0.05
1000	1652	0.80	0.97	449	1.20 ± 0.09
1200	1514	1.10	1.45	445	1.03 ± 0.27

The AC exhibits a BET surface area of 926 m<sup>2</sup>g<sup>-1</sup> and a pore volume of 0.65 mL g<sup>-1</sup>. Accordingly, a mean slit pore diameter of 1.40 nm results indicating the predominant presence of ultra- to supermicropores [31]. In contrast, the CDC materials

obtained at 800 and 1000 °C show a mainly ultramicroporous character, i.e., the MPD is below 1 nm. Consequently, the BET surface areas surpass the one of the AC reaching up to 1929 m<sup>2</sup>g<sup>-1</sup> for ZrC-CDC-800. The widely accepted trend of an increasing pore size with higher synthesis temperature gets clearer for the CDC materials produced at 1200 °C. For example, TiC-CDC-1200 has an MPD of 1.30 nm whereas it is 1.45 nm for ZrC-CDC-1200 and is therefore in the range of the AC. However, it should be mentioned that the BET surface area of the CDC materials is about 10 % (TiC-CDC-1200) to 60 % (ZrC-CDC-1200) higher than for the AC.

While the internal porosity *inter alia* determines how much MeOH can be principally accommodated, the amount of solid per volume and the microstructure of the carbon contribute to the overall (effective) thermal conductivity of the adsorbent bed. The resulting carbon microstructure for the different synthesis temperatures is assessed through Raman spectroscopy and indirectly via the onset for oxidation during temperature-programmed oxidation (TPO) (Figs. 1c and 1d). All Raman spectra are characterized by two more or less prominent peaks centered around 1335 and 1580 cm<sup>-1</sup> corresponding to the D and G band, respectively. Both bands get narrower and start to become separated with increasing synthesis temperature, which can be interpreted as hint for an enhanced microstructural ordering of the materials derived from both carbides. Moreover, TiC-CDC-1200 and ZrC-CDC-1200 give rise to a second-order Raman feature located at ca. 2664 cm<sup>-1</sup>, which is often referred to as 2D band. The occurrence of this band can be considered as additional hint for the change of the carbon microstructure towards a higher degree of ordering, although this is not directly reflected in the D over G intensity ratios.

Indeed, it seems that spatial resolution allows one to determine local differences in the carbon microstructure along the individual CDC particles, which is possible due to the relatively large particle size of the carbide powders in contrast to the analyzed spot size, but on the other hand makes this intensity ratio questionable as descriptor on the application level. Therefore, TPO was additionally chosen to characterize the carbon microstructure as it provides a more macroscopic picture of the sample. Fig. 1D depicts the mass loss curves for the AC and the CDC materials produced at 1000 °C. While increasing the measurement temperature, the samples pass through three regimes. Firstly, adsorbed species (probably water) desorb until ca. 200 °C giving rise to a minor weight loss. Secondly, the burn-off of the carbon skeleton proceeds between roughly 350 and 670 °C while only inorganic residues withstand the oxidizing atmosphere above 700 °C anymore. As a rule of thumb, it is reasonable to assume that more graphitic structures translate into an enhanced thermooxidative stability [23]. The onset temperature therefore can provide information about changes of the carbon microstructure, while the remaining mass after the TPO can be considered as an indicator for the purity of the carbon material.

The onset temperature is 439 °C for the AC and ca. 450 °C for the ZrC-CDCs independent of the synthesis temperature. As can be seen in Fig. 1D, the AC and ZrC-CDC-1000 exhibit an ash content of ca. 5 wt %, which is also the case for ZrC-CDC-800 and -1200 but not shown. In contrast, the CDC materials derived from TiC largely oxidize without possessing

any residues and the onset temperature increases from 421 to 563 °C for TiC-CDC-800 and -1200, respectively. On the basis of these results it can be inferred that (i) the carbon content (sorption active material) of the samples can be considered to be roughly equal and (ii) in particular TiC-CDC-1000 and -1200 exhibit an enhanced graphitic character compared to the rest of the carbon materials, which is expected to be beneficial in terms of thermal conductivity [32].

In essence, the chlorination of both carbide precursors at different temperatures yielded carbon materials with a broad range of BET surface areas and carbon microstructure. The surface areas of ZrC-CDC are extraordinary high, while the ones of TiC-CDC are closer to commercial ACs. Also, in terms of the PSD a closer match exists between the AC and TiC-CDC compared to the rather small-sized ZrC-CDC-1000. For the following study, where consolidated plates were produced, production parameters were varied, and an intensive characterization was carried out, the experimental matrix must be cut down to a manageable size. Due to the above-mentioned better similarity of TiC-CDC to AC it was decided to carry out this study with TiC-CDC material and the reference AC.

### 3.2 Carbon Plates without Heat Conductive Additives

Several dense plate-shaped adsorbent beds were prepared utilizing either 2 wt % CMC or 15 wt % PTFE as binder. Hereby, the properties of the active material (TiC-CDC) were varied in terms of the particle size fraction and by changing the chlorination temperature. The carbon composites were characterized by physisorption analysis assuming that the binder shows a negligible surface area itself and thus only adds extra mass to the system. It follows that the determined specific surface area is solely created from the porous carbon. The loss of BET surface area upon the shaping process is given (Fig. 2a).

During preparation of the carbon plates less than ca. 10 % of the initial BET surface area was lost indicating a high retention of the adsorption capacity. On the other hand, the pore size distributions accounting although for the voids between the particles (derived from Hg porosimetry) as depicted in Fig. 2b reveal that PTFE as binder gives rise to transport pores in the range of ca. 200–1200 nm, whereas even larger ones exceeding 1000 nm are obtained with CMC. Thus, the increase of the packing density obviously leads to an only minor extent of pore blocking but at the same time to the formation of interparticular macroporosity.

The effect of the interplay between binder and active material on the overall thermal conductivity of the carbon plates was further studied by transient hot bridge technique (THB; Fig. 2c). The following trends can be deduced: (i) Independent of the used binder, the AC-based carbon plates show the lowest effective thermal conductivity ( $\leq 0.16 \text{ W m}^{-1}\text{K}^{-1}$ ). (ii) When PTFE is used as binder, only a minor influence of the CDC carbon microstructure, as a consequence of the different synthesis temperatures, is observable for both particle fractions ( $\lambda_{\text{eff}} = 0.25\text{--}0.34 \text{ W m}^{-1}\text{K}^{-1}$ ). (iii) In contrast, when using CMC as binder, an enhancement of the graphitic character can be leveraged in

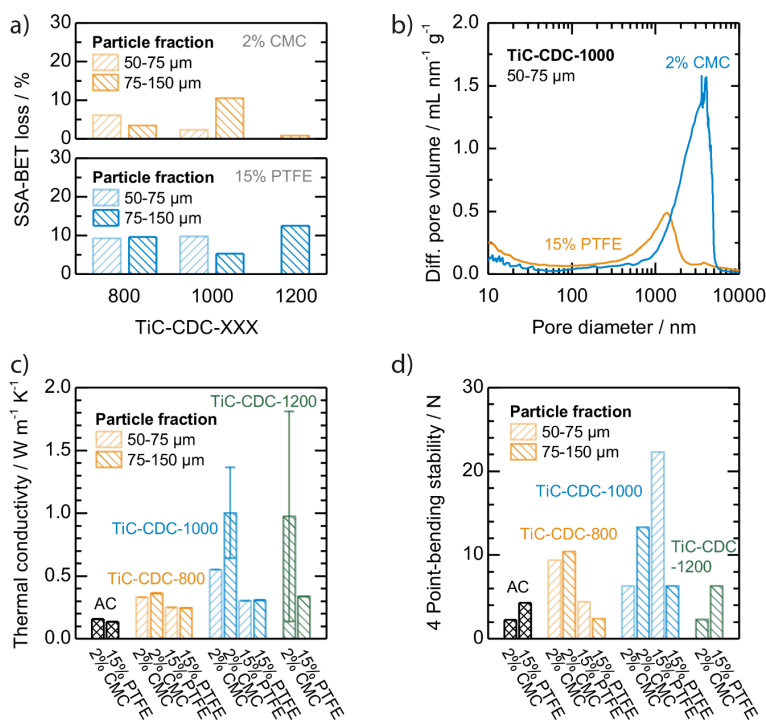


**Figure 2.** Activated carbon (AC), TiC-CDC-800, -1000, and -1200 plates using 2 wt % CMC or 15 wt % PTFE as binder. (a) Loss of BET surface area compared to the respective powdered material considering the additional binder mass; (b) volume-based pore size distribution obtained from Hg porosimetry. Influence of carbon material and binder on: (c) effective thermal conductivity, (d) mechanical stability.

terms of thermal conductivity in particular for the larger particle fraction (75–150 μm). However, it must be emphasized that the actual impact cannot be precisely determined for the highly conductive carbon plates based on TiC-CDC-1000 and -1200. The values are out of the measurement range of the device ( $> 1 \text{ W m}^{-1} \text{ K}^{-1}$ ) resulting in extremely large error bars, but which on the other hand also means an at least five times

higher effective thermal conductivity compared to the AC-based plates.

The type of binder in addition plays a pivotal role for the mechanical stability, which was tested in a 4-point bending setup. The results are illustrated in Fig. 2d. In general, CMC yields rigid but more brittle carbon plates, whereas PTFE-based ones are relatively flexible. Thus, no direct information about the binder influence can be drawn for a specific carbon material, instead the development of the mechanical stability needs to be seen in context of the series of TiC-CDC materials. It follows that at first glance carbon plates prepared from TiC-CDC-800 and -1000 are more stable than the ones using AC or TiC-CDC-1200. Secondly, it seems that there is an optimum of the CDC synthesis temperature (1000 °C), where PTFE as binder is most effective. Lastly, the more graphitic the CDC materials become, the lower gets the mechanical stability when using CMC. The only exception to this trend is the carbon plate made from TiC-CDC-1000 (75–150 μm). Thus, unlike for the thermal conductivity, no clear trend with respect to the properties of the CDC material and type of binder can be seen but it should be mentioned that all prepared carbon plates could be handled in the lab without excessive caution.

### 3.3 Carbon-Hybrid Plates with Heat-Conductive Additives

The influence of adding heat-conductive additives (HCAs) during the binder-based production process for the consolidated plates on the effective thermal conductivity was studied with TiC-CDC-1000 (50–75 μm). CMC and PTFE were used as binder, while BN, Ag, and graphite were added as HCAs with varying content from 10 to 50 wt %. The results of the material characterization are summarized in Figs. 3a–c.

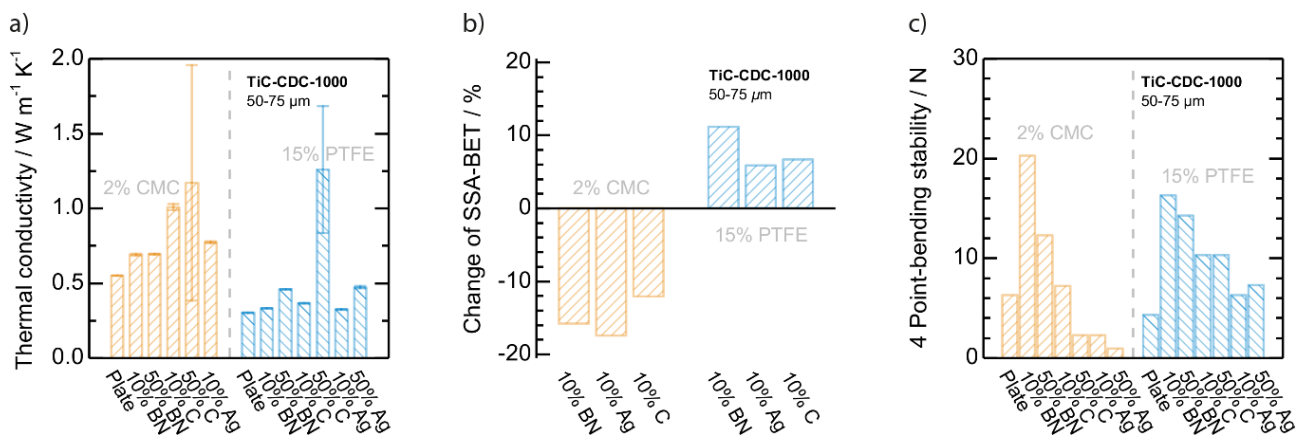


**Figure 3.** TiC-CDC-1000 (50–75 μm) plates using 2 wt % CMC or 15 wt % PTFE as binder. (a) Comparison of the effective thermal conductivity for different heat conductive additives and loadings; (b) change of the BET surface area due to the addition 10 wt % heat conductive additive compared to the unmodified plate (normalized to the active mass); (c) mechanical stability of different plates with and without additive.

When using CMC as binder, the addition of 10 wt % HCA increases the effective thermal conductivity from 0.55 to 0.69 (BN), 0.77 (Ag), and  $1.01 \text{ W m}^{-1} \text{ K}^{-1}$  (graphite). However, it seems that a higher HCA loading does not translate into a further improvement (50 wt % BN) or is at least not detectable anymore (50 wt % graphite). In contrast, for the carbon-hybrid plates made with PTFE, the higher HCA loading compared to the lower one results in an enhancement of the thermal conductivity of ca. 40 % for BN and Ag, respectively, whereas in the case of graphite, it increases by more than a factor of three. In other words, the percolation zone where an improvement of the thermal conductivity can be achieved by an increase of the HCA loading is much broader for PTFE compared to CMC, which, however, has the advantage of the higher thermal conductivities overall. Hereby, depending on the used binder the addition of 10 wt % (nonporous) HCA either reduces (CMC) or increases (PTFE) the BET surface area of the plates by ca. 10–15 % (Fig. 3b).

A side effect of the utilization of HCA is that for the PTFE-based carbon-hybrid plates the mechanical stability can increase by almost a factor of four (10 wt % BN; 16.3 N) compared to the unmodified plate (4.3 N). Indeed, using CMC as binder, also the highest stability is achieved when 10 wt % BN are added (20.3 N). However, unlike for PTFE in the case of CMC, Ag as HCA and a high graphite loading is detrimental in terms of mechanical stability.

### 3.4 Determination of Adsorption-Relevant Bed Parameters

Despite the prior presented material characterization, also data close to the aspired adsorption application were deduced. Therefore, methanol adsorption isotherms were recorded at 30 and 90 °C to derive the maximum MeOH capacity for several TiC-CDC-1000 (50–75 μm) plates with and without HCA. As an example, Fig. 4a presents the characteristic curve for the unmodified plate using 2 wt % CMC as binder, while the MeOH capacities normalized to the active mass (CDC) are summarized in Fig. 4b. It gets clear that the experimental data can be well fitted according to the Dubinin-Astakhov (D-A) equation in order to derive the MeOH capacity for the unmodified carbon plate, which is  $0.62 \text{ cm}^3 \text{ g}_{\text{CDC}}^{-1}$ .

It is noteworthy that in the case of CMC the addition of up to 50 wt % HCA virtually does not lower the MeOH capacity (<2 %) of the active material itself. The unmodified carbon plate prepared with PTFE also can take up  $0.62 \text{ cm}^3 \text{ g}_{\text{CDC}}^{-1}$ , which drops to  $0.52 \text{ cm}^3 \text{ g}_{\text{CDC}}^{-1}$  when adding 50 wt % Ag or graphite. The loss of MeOH capacity is, however, not surprising since the active material in the carbon-hybrid plate for these sam-

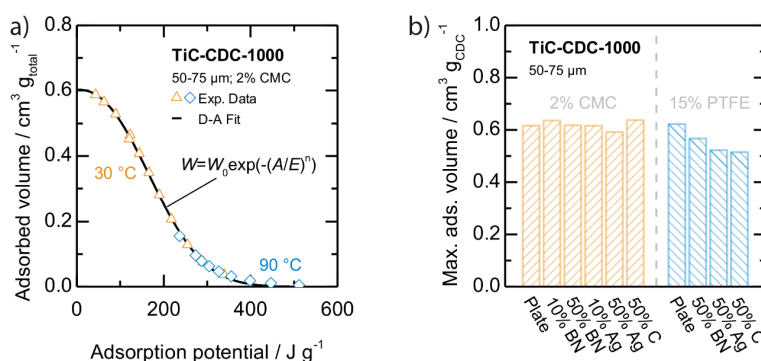


**Figure 4.** TiC-CDC-1000 (50–75 μm). (a) Characteristic curve for methanol using 2 wt % CMC as binder. The experimental data were fitted according to the Dubinin-Astakhov (D-A) equation. (b) Comparison of the MeOH capacity for different heat conductive additives and loadings (normalized to the active mass).

ples accounts to only 35 wt % anymore probably leading to a partial pore blocking.

In addition to the MeOH adsorption capacity, mainly characterized by the active material, the influence of the plate composition (particle fraction, binder, and additive) on the mass transport properties was studied in a simplified Wicke-Kallenbach Cell. The results are summarized in Tab. 2.

In general, plates prepared with TiC-CDC-1000 (50–75 μm) tend to have lower effective permeabilities ( $B_{0, \text{eff}}$ ) and Knudsen diffusivities ( $D_{\text{Kn, MeOH, const}}$ ) compared to the ones with larger particle size (75–150 μm). The results are in accordance with the common understanding that smaller voids between the particles (lower values for  $\varepsilon_p / \tau_{r_p}$ ) have a detrimental effect on the mass transport. Moreover, the utilization of additives additionally hampers the mass transport likely because the

**Table 2.** Summary of TiC-CDC-1000-based adsorption bed parameters. The data for the activated carbon are also included in the table for comparison.

Preparation of adsorption bed		Adsorption bed parameters				
Particle fraction [μm]	Binder [wt %]	Additive [wt %]	$W_0$ [ $\text{cm}^3 \text{ g}_{\text{CDC}}^{-1}$ ]	$\varepsilon_p / \tau_{r_p}$ [ $10^{-7} \text{ m}$ ]	$D_{\text{Kn, MeOH, const}}$ [ $10^{-6} \text{ m}^2 \text{ s}^{-1} \text{ K}^{-1/2}$ ]	$B_{0, \text{eff}}$ [ $10^{-14} \text{ m}^2$ ]
<i>TiC-CDC-1000</i>						
50–75	2 % CMC	–	0.62	1.51	2.59	5.06
50–75	2 % CMC	10 % BN	0.64	0.89	1.52	2.74
50–75	2 % CMC	50 % BN	0.62	0.04	0.06	0.01
50–75	2 % CMC	10 % C	–	1.27	2.16	3.82
50–75	20 % PTFE	–	0.65	1.98	3.37	7.97
75–150	2 % CMC	10 % BN	–	1.91	3.27	11.16
75–150	5 % CMC	–	0.61	2.36	4.04	13.17
<i>AC</i>						
< 115	10 % CMC	–	0.37 <sup>a)</sup>	0.52	0.89	1.24

<sup>a)</sup>The MeOH capacity is normalized to the mass of activated carbon.

interparticular porosity is further reduced. As can be observed for the plate TiC-CDC-1000 (50–75  $\mu\text{m}$ ; 2 wt % CMC; 50 wt % BN), this effect can even lower the mass transport properties by about two orders of magnitude. In other words, the high amount of BN particles on the one hand increases the effective thermal conductivity (Fig. 3a) and mechanical stability (Fig. 3c) compared to the unmodified plate but on the other hand clogs the transport pores to a large extent clearly revealing the influence of the competing properties.

## 4 Conclusion

Carbon plates for the application in carbon-MeOH adsorption cooling systems were prepared via a cold-pressing approach using CDCs derived from TiC or ZrC as model active materials with tailorable properties. The utilization of CMC as binder yielded more brittle carbon plates, whereas the PTFE-based ones were relatively flexible. The thermal conductivity of the unmodified carbon plates could be enhanced by using different heat-conductive additives and loadings. As a side effect, the utilization of in particular 10 wt % BN as HCA greatly improved the mechanical stability of the plates but did not lead to a disproportionate drop of the MeOH adsorption capacity.

These findings and the vast data set for the different materials shows the parameter space, which is accessible for AC plates produced through a binder-based shaping process with optional addition of heat-conductive agents. This is the basis for a follow-up study dealing with a simulative approach in order to target the interplay of material properties and process conditions for the optimization of adsorptive heat pump systems.

## Supporting Information

Supporting Information for this article can be found under DOI: <https://doi.org/10.1002/ceat.202000181>.

## Acknowledgment

The authors gratefully acknowledge the funding of the German Research Council (DFG) within the DFG projects NI 932/10-1 and ET 101/11-1. In addition, we would like to thank P. Schmatz for the assistance with the Raman spectroscopy and the nitrogen physisorption analysis and the group of Prof. J. Schneider for the help with the mercury porosimetry measurements. Open access funding enabled and organized by Projekt DEAL.

*The authors have declared no conflict of interest.*

## Symbols used

$A$	$[\text{J g}^{-1}]$	adsorption potential
$B_{0,\text{eff}}$	$[10^{-14} \text{m}^2]$	effective permeability
$D_{\text{Kn,MeOH,const}}$	$[10^{-6} \text{m}^2 \text{s}^{-1} \text{K}^{-1/2}]$	temperature-independent part of the Knudsen diffusion coefficient for MeOH

$E$	$[\text{J g}^{-1}]$	characteristic energy of one adsorbate
$I$	$[-]$	intensity (counts)
MPD	$[\text{nm}]$	mean pore diameter (assuming a slit pore geometry)
$n$	$[-]$	surface heterogeneity
$r_p$	$[\text{nm}]$	radius of the transport pores
SSA-BET	$[\text{m}^2 \text{g}^{-1}]$	specific surface area determined via the Brunauer-Emmett-Teller multipoint method
$T$	$[^\circ\text{C}]$	temperature
$V_{\text{pore}}$	$[\text{mL g}^{-1}]$	pore volume
$W$	$[\text{cm}^3 \text{g}_{\text{CDC}}^{-1}]$	adsorbed volume of MeOH
$W_0$	$[\text{cm}^3 \text{g}_{\text{CDC}}^{-1}]$	maximum absorbable volume of MeOH

### Greek letters

$\varepsilon_p$	$[-]$	interparticular porosity
$\lambda_{\text{eff}}$	$[\text{W m}^{-1} \text{K}^{-1}]$	effective thermal conductivity
$\tau$	$[-]$	tortuosity
$\Phi$	$[\text{Vol } \%]$	volume fraction

### Sub- and superscripts

CDC	normalized to the active mass (CDC)
D	D band
G	G band
Onset	onset temperature for the oxidation
total	normalized to the overall mass (active material, binder, additive)

### Abbreviations

AC	activated carbon
Ag	silver
BN	boron nitride
C	carbon (here in the modification of graphite)
CDC	carbide-derived carbon
CMC	carboxymethyl cellulose
COP	coefficient of performance
MPD	mean pore diameter
PTFE	polytetrafluoroethylene
SEM	scanning electron microscopy
TiC	titanium carbide
TPO	temperature-programmed oxidation
ZrC	zirconium carbide

## References

- [1] A. A. Askalany, M. Salem, I. M. Ismael, A. H. H. Ali, M. G. Morsy, B. B. Saha, *Renewable Sustainable Energy Rev.* **2013**, *19*, 565–572. DOI: <https://doi.org/10.1016/j.rser.2012.11.037>
- [2] I. I. El-Sharkawy, A. Pal, T. Miyazaki, B. B. Saha, S. Koyama, *Appl. Therm. Eng.* **2016**, *98*, 1214–1220. DOI: <https://doi.org/10.1016/j.applthermaleng.2015.12.105>

- [3] T. Miyazaki, A. Akisawa, B. B. Saha, I. I. El-Sharkawy, A. Chakraborty, *Int. J. Refrig.* **2009**, *32* (5), 846–853. DOI: <https://doi.org/10.1016/j.ijrefrig.2008.12.002>
- [4] Y. I. Aristov, A. Sapienza, D. S. Ovoshchnikov, A. Freni, G. Restuccia, *Int. J. Refrig.* **2012**, *35* (3), 525–531. DOI: <https://doi.org/10.1016/j.ijrefrig.2010.07.019>
- [5] I. I. El-Sharkawy, H. AbdelMeguid, B. B. Saha, *Int. J. Heat Mass Transfer* **2013**, *63*, 171–182. DOI: <https://doi.org/10.1016/j.ijheatmasstransfer.2013.03.076>
- [6] Y. I. Aristov, G. Restuccia, G. Cacciola, V. N. Parmon, *Appl. Therm. Eng.* **2002**, *22* (2), 191–204. DOI: [https://doi.org/10.1016/S1359-4311\(01\)00072-2](https://doi.org/10.1016/S1359-4311(01)00072-2)
- [7] Q. Cui, G. Tao, H. Chen, X. Guo, H. Yao, *Energy* **2005**, *30* (2), 261–271. DOI: <https://doi.org/10.1016/j.energy.2004.05.005>
- [8] I. I. El-Sharkawy, K. Kuwahara, B. B. Saha, S. Koyama, K. C. Ng, *Appl. Therm. Eng.* **2006**, *26* (8), 859–865. DOI: <https://doi.org/10.1016/j.applthermaleng.2005.10.010>
- [9] İ. Solmuş, C. Yamalı, B. Kaftanoğlu, D. Baker, A. Çağlar, *Appl. Energy* **2010**, *87* (6), 2062–2067. DOI: <https://doi.org/10.1016/j.apenergy.2009.11.027>
- [10] S. K. Henninger, F. P. Schmidt, H. M. Henning, *Appl. Therm. Eng.* **2010**, *30* (13), 1692–1702. DOI: <https://doi.org/10.1016/j.applthermaleng.2010.03.028>
- [11] S. K. Henninger, F. Jeremias, H. Kummer, P. Schossig, H.-M. Henning, *Energy Procedia* **2012**, *30*, 279–288. DOI: <https://doi.org/10.1016/j.egypro.2012.11.033>
- [12] Y. I. Aristov, *Appl. Therm. Eng.* **2013**, *50* (2), 1610–1618. DOI: <https://doi.org/10.1016/j.applthermaleng.2011.09.003>
- [13] K. Uddin, I. I. El-Sharkawy, T. Miyazaki, B. B. Saha, S. Koyama, H.-S. Kil, J. Miyawaki, S.-H. Yoon, *Appl. Therm. Eng.* **2014**, *72* (2), 211–218. DOI: <https://doi.org/10.1016/j.applthermaleng.2014.03.062>
- [14] I. I. El-Sharkawy, K. Uddin, T. Miyazaki, B. B. Saha, S. Koyama, J. Miyawaki, S.-H. Yoon, *Int. J. Heat Mass Transfer* **2014**, *73*, 445–455. DOI: <https://doi.org/10.1016/j.ijheatmasstransfer.2014.02.046>
- [15] I. I. El-Sharkawy, K. Uddin, T. Miyazaki, B. Baran Saha, S. Koyama, H.-S. Kil, S.-H. Yoon, J. Miyawaki, *Int. J. Heat Mass Transfer* **2015**, *81*, 171–178. DOI: <https://doi.org/10.1016/j.ijheatmasstransfer.2014.10.012>
- [16] M. M. Younes, I. I. El-Sharkawy, A. E. Kabeel, B. B. Saha, *Appl. Therm. Eng.* **2017**, *114*, 394–414. DOI: <https://doi.org/10.1016/j.applthermaleng.2016.11.138>
- [17] G. Cacciola, G. Restuccia, L. Mercadante, *Carbon* **1995**, *33* (9), 1205–1210. DOI: [https://doi.org/10.1016/0008-6223\(95\)00051-E](https://doi.org/10.1016/0008-6223(95)00051-E)
- [18] Z. Tamainot-Telto, R. E. Critoph, *Appl. Therm. Eng.* **2001**, *21* (1), 37–52. DOI: [https://doi.org/10.1016/S1359-4311\(00\)00030-2](https://doi.org/10.1016/S1359-4311(00)00030-2)
- [19] V. Presser, M. Heon, Y. Gogotsi, *Adv. Funct. Mater.* **2011**, *21* (5), 810–833. DOI: <https://doi.org/10.1002/adfm.201002094>
- [20] S. Urbonaite, S. Wachtmeister, C. Mirguet, E. Coronel, W. Y. Zou, S. Csillag, G. Svensson, *Carbon* **2007**, *45* (10), 2047–2053. DOI: <https://doi.org/10.1016/j.carbon.2007.05.022>
- [21] S. Urbonaite, J. M. Juárez-Galán, J. Leis, F. Rodríguez-Reinoso, G. Svensson, *Microporous Mesoporous Mater.* **2008**, *113* (1–3), 14–21. DOI: <https://doi.org/10.1016/j.micromeso.2007.10.046>
- [22] S. Urbonaite, L. Hålldahl, G. Svensson, *Carbon* **2008**, *46* (14), 1942–1947. DOI: <https://doi.org/10.1016/j.carbon.2008.08.004>
- [23] J. Gläsel, J. Diao, Z. Feng, M. Hilgart, T. Wolker, D. S. Su, B. J. M. Etzold, *Chem. Mater.* **2015**, *27* (16), 5719–5725. DOI: <https://doi.org/10.1021/acs.chemmater.5b02262>
- [24] R. K. Dash, G. Yushin, Y. Gogotsi, *Microporous Mesoporous Mater.* **2005**, *86* (1–3), 50–57. DOI: <https://doi.org/10.1016/j.micromeso.2005.05.047>
- [25] A. Gorbach, M. Stegmaier, G. Eigenberger, *Adsorption* **2004**, *10* (1), 29–46. DOI: <https://doi.org/10.1023/B:ADSO.0000024033.60103.ff>
- [26] E. Wicke, R. Kallenbach, *Kolloid-Z.* **1941**, *97* (2), 135–151. DOI: <https://doi.org/10.1007/bf01502640>
- [27] E. A. Mason, A. P. Malinauskas, R. B. Evans, *J. Chem. Phys.* **1967**, *46* (8), 3199–3216. DOI: <https://doi.org/10.1063/1.1841191>
- [28] Z. G. Cambaz, G. N. Yushin, Y. Gogotsi, K. L. Vyshnyakova, L. N. Pereselentseva, *J. Am. Ceram. Soc.* **2006**, *89* (2), 509–514. DOI: <https://doi.org/10.1111/j.1551-2916.2005.00780.x>
- [29] J. Jia, A. Zhou, Y. Zhu, J. Liu, S. Feng, Y. Tao, B. Xing, C. Zhang, *J. Nanomater.* **2015**, Article 125. DOI: <https://doi.org/10.1155/2015/163415>
- [30] A. Silvestre-Albero, S. Rico-Francés, F. Rodríguez-Reinoso, A. M. Kern, M. Klumpp, B. J. M. Etzold, J. Silvestre-Albero, *Carbon* **2013**, *59*, 221–228. DOI: <https://doi.org/10.1016/j.carbon.2013.03.012>
- [31] M. Thommes, *Chem. Ing. Tech.* **2010**, *82* (7), 1059–1073. DOI: <https://doi.org/10.1002/cite.201000064>
- [32] A. M. Kern, B. Zierath, J. Haertlé, T. Fey, B. J. M. Etzold, *Chem. Eng. Technol.* **2016**, *39* (6), 1121–1129. DOI: <https://doi.org/10.1002/ceat.201600011>